Available online at www.sciencedirect.com

ScienceDirect

Energy Procedia 125 (2017) 494–503

Energy Procedia

www.elsevier.com/locate/procedia

European Geosciences Union General Assembly 2017, EGU Division Energy, Resources & Environment, ERE

Caprock Integrity and Induced Seismicity from Laboratory and Numerical Experiments

Victor Vilarrasa[a,b,*], Roman Y. Makhnenko[c]

[a]*Institute of Environmental Assessment and Water Research, Spanish National Research Council (IDAEA-CSIC), Barcelona, Spain*
[b]*Associated Unit: Hydrogeology Group (UPC-CSIC), Barcelona, Spain*
[c]*Department of Civil & Environmental Engineering, University of Illinois at Urbana-Champaign, USA*

Abstract

CO_2 leakage is a major concern for geologic carbon storage. To assess the caprock sealing capacity and the strength of faults, we test in the laboratory the rock types involved in CO_2 storage at representative in-situ conditions. We use the measured parameters as input data to a numerical model that simulates CO_2 injection in a deep saline aquifer bounded by a low-permeable fault. We find that the caprock sealing capacity is maintained and that, even if a fault undergoes a series of microseismic events or aseismic slip, leakage is unlikely to occur through ductile clay-rich faults.

Peer-review under responsibility of the scientific committee of the European Geosciences Union (EGU) General Assembly 2017 – Division Energy, Resources and the Environment (ERE).

Keywords: CO_2 storage; reservoir behavior; geomechanics; breakthrough pressure; relative permeability; fault reactivation; CO_2 leakage

1. Introduction

The success of geo-energy applications requires a good understanding of the coupled thermo-hydro-mechanical-chemical processes that occur in the subsurface as a result of fluid injection. To advance in this understanding, it is crucial for predictive numerical models to use realistic rock properties obtained from laboratory experiments.

* Corresponding author. Tel.: +34 93 400 61 00
E-mail address: victor.vilarrasa@idaea.csic.es

1876-6102
Peer-review under responsibility of the scientific committee of the European Geosciences Union (EGU) General Assembly 2017 – Division Energy, Resources and the Environment (ERE).
10.1016/j.egypro.2017.08.172

However, given the difficulties to reproduce in the laboratory the pressure and temperature conditions representative of geo-energy applications, i.e., between several hundreds of meters to a few kilometers deep, data availability is scarce. Thus, a large number of numerical studies had to assume approximate values of rock properties to identify the relevant processes related to geo-energies, e.g. [1-3]. Nevertheless, generic studies are useful to improve process understanding.

Despite the limitations for high pressure and temperature testing, recent developments have allowed to test rock samples at representative in-situ conditions, e.g. [4,5]. On the one hand, sedimentary rock, such as sandstone and limestone, is of interest for fluid injection related to CO_2 storage and wastewater disposal because of its relatively high permeability, which hinders excessive overpressure [6]. On the other hand, crystalline rock is important for enhanced geothermal systems [7] and to understand seismicity induced by fluid injection in overlying sedimentary rock [8].

The use of rock properties from actual laboratory measurements is of interest to model the behavior of the subsurface at a specific site. In particular, accurate measurements of rock properties are required to design field experiments, decide the location of monitoring wells, and define the maximum sustainable injection pressure in pilot, demonstration, and industrial scale projects. These laboratory measurements should be accompanied by field characterization to account for scale effects on rock properties.

In this study, we measure properties of both sedimentary and crystalline rock and use these measured properties to assess caprock and fault stability associated with CO_2 injection. We measure two-phase flow and geomechanical properties of (*i*) Berea sandstone, which is a high-permeable sedimentary rock representative of storage formations, (*ii*) intact and remolded Opalinus clay, which are representative of caprock and faulted material, respectively, and (*iii*) hydro-mechanical properties of Charcoal granite, which is a representative of the crystalline basement. We model a geological setting including a stratified sedimentary basin with alternating low- and high-permeable layers and the crystalline basement at the bottom. The model includes a normal fault with a non-negligible offset. The fault is composed of a low-permeable fault core and a damaged zone on each side of the core. We analyze how the overpressure induced by CO_2 injection affects both caprock and fault stability.

2. Experimental methods

2.1. Material

We consider Berea sandstone, Opalinus clay (shale), and Charcoal granite to be the representatives of reservoir, caprock, and basement, respectively, and we measure their properties in the lab. Berea sandstone is a quartz-rich (>90%) sedimentary rock with porosity of 0.23, permeability $k \sim 10^{-14}$ m^2, and slight degree of elastic anisotropy (5-7%). Opalinus clay, a Jurassic shale from Switzerland, is taken as a ductile clay-rich (>55% of clay minerals) and low-permeable ($k \sim 10^{-21}$ m^2) cap and base rock representative. Its porosity is 0.12 and its elastic anisotropy is about 20-30%. Additionally, its permeability along and perpendicular to the bedding planes differ by a factor of 3. The crystalline basement is assumed to be formed by Charcoal granite ($k \sim 10^{-20}$ m^2), with 0.015 porosity that consists mainly of open cracks, which also determine a high level of elastic anisotropy (up to 100%) [9]. To represent the fault core, we test reconstituted to less than 0.5 mm grains Opalinus clay powder that is subsequently saturated with brine and consolidated at mean stresses above 20 MPa (referred here as "remolded shale"), which is isotropic in terms of elastic properties and permeability. At simulated reservoir conditions, porosity of fault core is 0.15 and permeability is $k \sim 10^{-20}$ m^2. Mercury intrusion porosimetry tests are performed on non-damaged rock samples with characteristic size of 8mm and show that the dominant pore throat diameter for the reservoir rock is about 30 micron, while those for shale (0.015 micron), remolded shale (0.015 micron), and granite (0.009 micron) are three orders of magnitude smaller, which lead to low-permeability and strong capillary effects in these formations (Figure 1). Pore size distribution and knowledge of contact angles and interfacial tensions can also provide an evaluation of pore entry pressures for CO_2 for low-permeable formations.

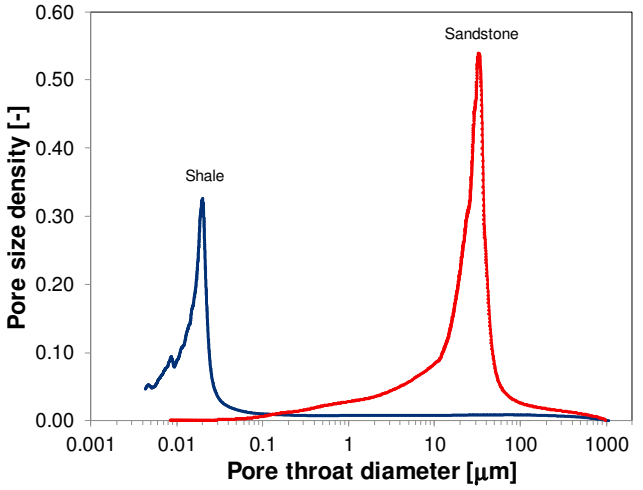

Fig. 1. Pore size distribution for the sandstone (reservoir rock) and shale (caprock).

2.2. Geomechanical and hydraulic properties

Poroelastic and failure characteristics of the materials under consideration are measured in conventional triaxial experiments with specimens of 50 mm in diameter and 100 mm in height at effective mean stresses corresponding to 1.0-1.5 km depth, with vertical effective stress ranging from 15 to 28 MPa and horizontal effective stress ranging from 10 to 18 MPa. Drained and undrained poroelastic parameters are reported for Berea sandstone [10], Opalinus clay (shale) [11], and remolded shale [12] fully saturated with brine. Failure characteristics (friction and cohesion) of the sandstone and remolded shale are calculated from triaxial strength tests performed under drained (for sandstone) and undrained (remolded shale) conditions. Failure properties of shale and granite are adopted from the literature [13,14], as well as the elastic properties of the granite [9].

The critical parameters for the barrier sealing efficiency is the capillary breakthrough or gas entry pressure, i.e., the excess of non-wetting fluid (e.g., CO_2) pressure above the initial pore fluid pressure that is enough to initiate its flow through a low-permeable rock. This parameter can be estimated from mercury intrusion porosimetry tests, but often times only with an order of the magnitude accuracy [15]. Tests on thin (12 mm in height and 35 mm in diameter) shale and remolded shale specimens loaded under oedometric conditions allow evaluating the breakthrough pressure and permeability for liquid and supercritical CO_2. The breakthrough pressure is measured using two different methods: direct (with the establishment of continuous CO_2 flow) and indirect (through a residual capillary pressure evaluation) [5,16,17]. Breakthrough pressure for the sandstone is also measured in a conventional triaxial configuration. Granite CO_2 entry pressure is evaluated from the knowledge of the dominant pore throat diameter.

Relative CO_2 permeability is an important parameter for predicting flow in reservoir and it is measured in steady-state flow tests performed at fixed differential pressures. Upstream and downstream pressure-volume controllers are utilized to induce the pore pressure inside the rock and measure the volume of fluid that entered or left the sample. A syringe pump (Teledyne ISCO, USA) is connected in parallel with the upstream pressure-volume controller and is used to inject CO_2 into the sample, either as a single phase or in combination with water (or brine) from upstream pressure-volume controller, providing two-phase flow with controlled fraction of each phase. The upstream and downstream pressure transducers provide pore pressure. From Darcy's law, the relative permeability of α–phase can be estimated as

$$k_{r\alpha} = -\frac{4\Delta V_\alpha \, \mu_\alpha}{\pi \, D^2 \Delta t \, k\left(\frac{\Delta p_\alpha}{L} + \rho_\alpha g\right)}, \qquad \alpha = c, w \tag{1}$$

where ΔV_α is the increment of outflow volume of α–phase (c = CO_2 and w = water), μ_α is the α–phase viscosity, D is the sample diameter, Δt is the increment of time, Δp_α is the pressure difference across the sample, L is the sample

length, ρ_α is α–phase density, and g is gravity. In case of single-phase flow, the effective permeability (i.e., the product of the intrinsic and the relative permeability) is equal to the intrinsic permeability that is measured before CO_2 injection during the flow of a saturating fluid. Degree of residual water saturation is evaluated from the difference between inflow and outflow CO_2 fractions. The latter one is calculated from the compressibility of the downstream fluid precisely calibrated for different CO_2 - water (saturated with CO_2) ratios at given temperatures and pressures.

3. Numerical methods

3.1. Model geometry

We model a horizontal sedimentary basin where low-permeable formations with high capillary entry pressure alternate with high-permeable geologic formations (Figure 2). These sedimentary rocks are placed on top of the crystalline basement. The storage formation, which top is placed at a depth of 1.5 km, is overlaid and underlain by low-permeable layers, so the crystalline basement is not directly affected by the overpressure induced by CO_2 injection. We assign to the storage formation the properties of Berea sandstone, to the low-permeable sedimentary formations the properties of Opalinus clay (shale), and to the basement the properties of Charcoal granite. Such properties are described in Sections 2.1 and 4.

Our model includes a normal fault that has an offset of 25 m. The fault is composed by a low-permeable fault core, which is surrounded by a damage zone on both sides of the fault. While the fault core has constant properties along the fault, the damage zone has different properties depending on the rock it is in contact with. To avoid boundary effects, the model extends laterally 15 km on both sides of the fault. Given the symmetry of the problem, the model has 2D plane strain conditions.

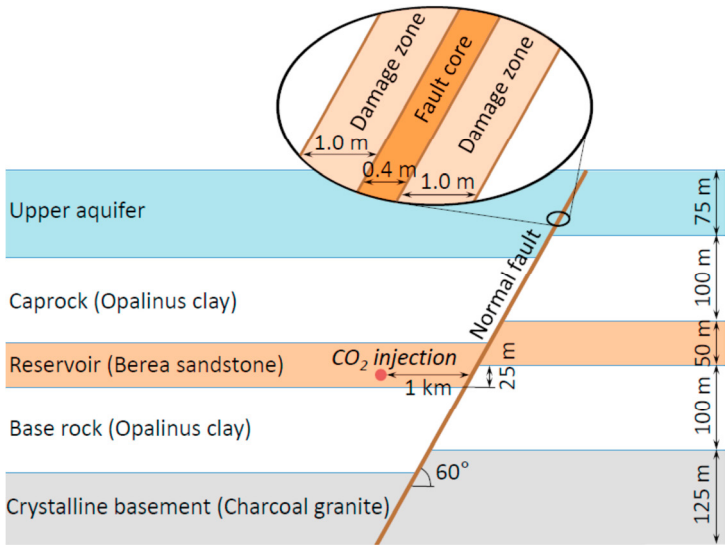

Fig. 2. Schematic representation of the model geometry.

3.2. Numerical model

Initially, pore pressure is hydrostatic. The boundary conditions are constant pressure on both sides of the model. However, given the time scale of the simulation, i.e., around half a year of CO_2 injection, the pressure perturbation front does not reach the boundaries. Thus, the nature of the boundary condition does not have any effect on the results. CO_2 is injected through a horizontal well at a rate of $2 \cdot 10^{-3}$ kg/s/m at the bottom of the storage formation.

The initial stress state corresponds to a normal faulting stress regime. The vertical stress has a gradient given by the weight of the rock, which is equal to 23 MPa/km. The horizontal to vertical stress ratio is assumed to be equal to 0.7. This ratio yields a mobilized friction coefficient of 0.4, which is within the range of values found in sedimentary formations [18]. Boundary conditions are constant stress equal to the overburden on the top boundary and no displacement perpendicular to the boundary on the other boundaries. We consider an elasto-plastic behavior of all geomaterials.

We solve this two-phase flow problem in a deformable porous media using the numerical code CODE_BRIGHT [19], which has been extended to simulate CO_2 injection [20]. CODE_BRIGHT is a fully coupled finite element code that solves flow and mechanical equations in a fully coupled way. The mesh is made of quadrilateral elements, with a higher refinement around the fault and the injection well.

4. Rock properties

4.1 Reservoir rock

Supercritical CO_2 retention curve for water-saturated Berea sandstone is calculated from its pore size distribution and is presented in Figure 3a. Additionally, gaseous CO_2 retention curve is measured in a conventional triaxial configuration with ceramic disks that allow accurate control of wetting and non-wetting fluid pressures and replaced water volume. Even though there is a certain difference between the observed and measured curves, possibly caused by different utilized CO_2 phases, both methods show very low (below 0.02 MPa) CO_2 entry pressure for the sandstone. The relative permeability curves are obtained for liquid (20 °C) and supercritical CO_2 (39 °C) flow in Berea sandstone. For the case of maximum achieved CO_2 saturation (about 60%), relative permeability of liquid CO_2 is found to be $k_{rc} = 0.12$, which is 20% larger than the one at supercritical state (Figure 3b). The flow rates through a high-permeable rock are limited by the upstream and downstream controllers and provide a maximum measurable degree of CO_2 saturation of 60% for pure CO_2 flow in water-saturated sandstone. Nonetheless, the measured retention curve in Figure 3a shows that it can be above 70% at elevated non-wetting fluid pressures.

Measured relative CO_2 permeability for liquid and supercritical phases are within the reported ranges for high-permeable rock (~10^{-14}–10^{-13} m^2) close to the residual water saturation, i.e., k_{rc} = 0.05-0.20 [21]. Slightly different curves are obtained for relative permeability of water given that the non-wetting fluid can be either CO_2 in liquid or supercritical states. The results are fitted using the van Genuchten [22] model

$$k_{rw} = \sqrt{S_w^*}\left\{1-\left(1-\left[S_w^*\right]^{1/m}\right)^m\right\}^2, \tag{2}$$

providing the best fit for a m-parameter equal to 0.80 at 39 °C and equal to 0.78 at 20 °C. Our measurements around $S_{H2O} = 0.6$ do not show the monotonic increase predicted by this model, which has to be explored further.

The diffusivity coefficient of high-permeable sandstone is on the order of 0.1 m^2/s [23], which determines quick equilibration of pore pressure within the formation (on the order of hours for a 50-meter-thick layer), hence drained response can be assumed. Drained Young's modulus of Berea sandstone is measured to be E = 14.0 MPa and Poisson's ratio is ν = 0.31 [10]. A series of triaxial compression tests are conducted under dry, drained, and undrained conditions, and provide consistent values of the friction angle $\phi = 42^o$ and cohesion c = 9 MPa [24]. Study of CO_2 interaction with sandstone shows no measurable stiffness changes (after three weeks of CO_2 flow). It is explained mainly due to low calcite and clay concentration in the material (about 1%) [25]. However, the intrinsic permeability of the sandstone samples after CO_2 treatment shows a slight increase (2-4%).

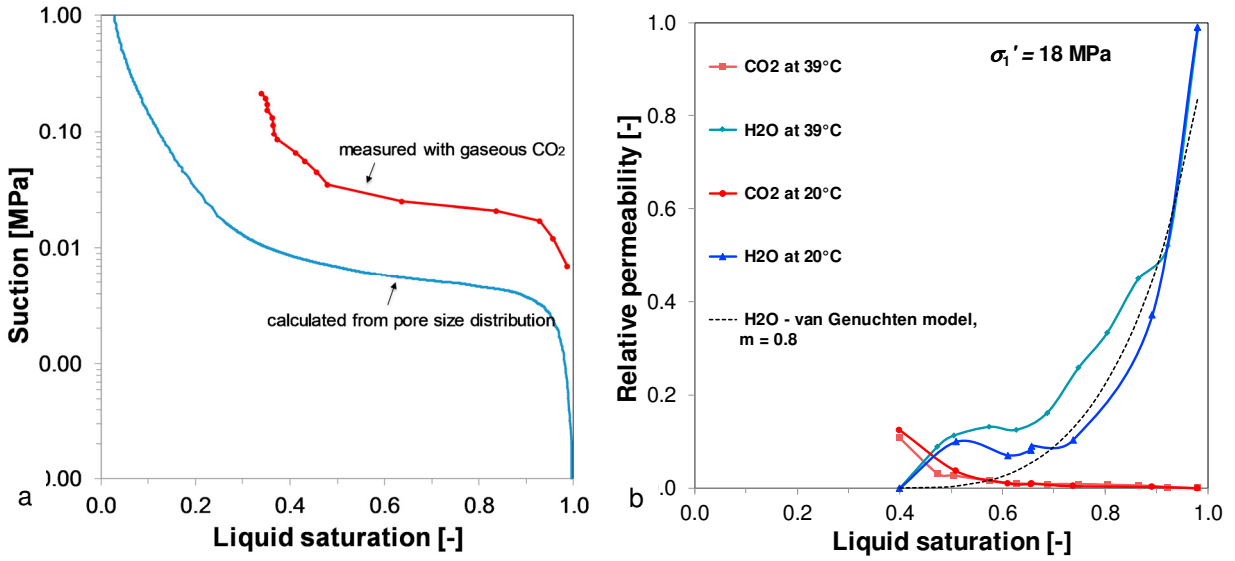

Figure 3. (a) Water retention curves for Berea sandstone obtained from pore size distribution for supercritical CO_2 and direct measurements with gaseous CO_2 as a non-wetting fluid. (b) Relative permeability for water and CO_2 at 20 ºC and 39 ºC as a function of water saturation.

4.2. Caprock, basement, and fault material

CO_2 breakthrough pressures for reservoir rock (sandstone), fault core (remolded shale) and cap and base rock (intact shale) are presented in Figure 4. For the range of stresses considered in the model, the breakthrough pressure is measured to be 0.02 MPa for the sandstone, 9-10 MPa for intact shale, and 3-5 MPa for the remolded material. The gas entry pressure for crystalline basement is estimated from pore size distribution to be around 12 MPa. CO_2 effective permeability (i.e., intrinsic permeability times CO_2 relative permeability) of brine-saturated shale is at least an order of magnitude smaller than the one for brine and is ~ 10^{-22} m^2 for the intact and reconstituted material loaded to in-situ conditions [5]. High differential pressures need to be applied to address relative CO_2 permeability in low-permeable clays with strongly stress-dependent flow properties. The maximum CO_2 saturation at 16 MPa differential pressure was measured to be 0.2 for fault core and 0.12 for cap and base rock, so the overall permeability curves could not be derived. Relative CO_2 and water permeability curves are taken as power functions of saturation, with a power of 6 for the shale, remolded shale, and granite [26]. van Genuchten's [22] shape parameter is assumed to be $m = 0.3$ for the low-permeable formations under consideration.

The characteristic pressure diffusion time across the fault core is about two days, which is two orders of magnitude smaller than the considered injection time (0.5 years), hence the drained response is assumed. Drained Young's modulus of the fault core is strongly stress-dependent and is equal to $E = 1.4$ GPa at simulated conditions and drained Poisson's ratio is $\nu = 0.30$. Drained elastic properties are also reported for the crystalline basement, $E = 55$ GPa and $\nu = 0.18$ [9], with the characteristic diffusion time in the order of a few weeks. Conversely, the undrained (short-term) elastic parameters are reported for the confining layers (shale) due to their characteristic timescale of the diffusion processes being on the order of tens of years. The undrained Young's modulus of Opalinus clay is $E_u = 3.0$ GPa and Poisson's ratio $\nu_u = 0.40$. Cohesion and friction angles are $c = 5$ MPa, $\phi = 24º$ and $c = 60$ MPa, $\phi = 42º$ MPa for intact shale cores loaded perpendicular to the bedding planes in brittle regime and crystalline basement, respectively [13,14]. Cohesion and friction for the fault core are determined from undrained triaxial compression data in the brittle regime, $c = 0.1$ MPa and $\phi = 24º$, with the same friction angle for both intact and remolded Opalinus clay.

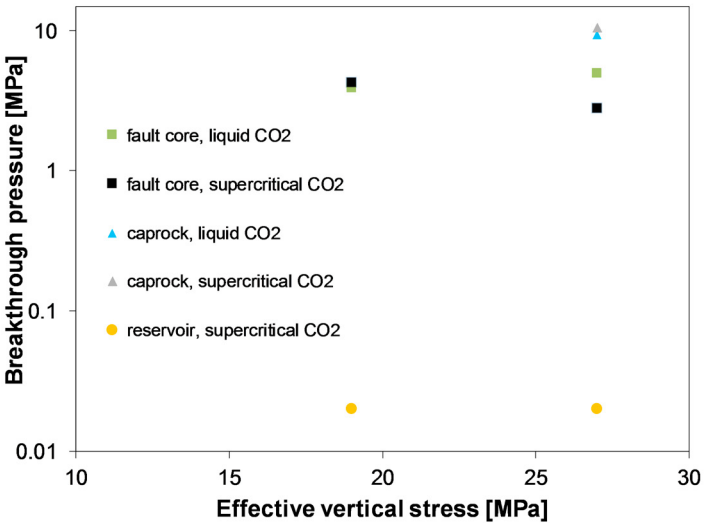

Figure 4. Measured CO_2 breakthrough pressures: liquid (blue triangles) and supercritical (grey triangles) CO_2 in shale (caprock), liquid (green squares) and supercritical (black squares) CO_2 in remolded shale (fault), and supercritical CO_2 (yellow circles) in reservoir rock (sandstone).

5. CO_2 injection model

5.1. Fluid pressure evolution

CO_2 injection through a horizontal well induces a fluid pressure that increases monotonically with time [27,28]. This pressure buildup is accentuated by the presence of the low-permeable fault, which induces an additional overpressure in the region between the injection well and the fault. After around half a year of injection, overpressure is 5.6 MPa next to the fault and 6.3 MPa at the injection well. In contrast to the monotonic pressure increase that occurs in the reservoir, fluid pressure initially drops in the caprock by 0.6 MPa, before starting to increase after one month of injection. After half a year of injection, pressure buildup in the lower portion of the caprock, above the injection well, is 0.9 MPa. This pore pressure evolution in low-permeable formations as a response to fluid injection in underlying permeable layers is known as reverse-water level fluctuation or Noordbergum effect [29] and controls caprock stability.

5.2. Caprock integrity

The most critical zone of the caprock is around injection wells, where overpressure is maximum. However, given the low permeability of caprock, overpressure propagation into it is significantly hindered. Furthermore, poromechanical effects lead to a reverse-water level fluctuation in the caprock (see Section 5.1), which improves caprock stability in the short term (see the Mohr circle corresponding to 56 days in Figure 5). Subsequently, once fluid pressure starts to progressively build up in the caprock, the Mohr circle is displaced towards the failure surface. However, the horizontal total stresses increase in the lower portion of the caprock as a response to pressure buildup, which reduces the deviatoric stress, and thus, caprock stability improves. Figure 5 illustrates that caprock stability is maintained in the long term, as shown by the reduced size of the Mohr circle corresponding to 160 days of injection. Actually, the mobilized friction coefficient is lower at the end of injection than prior to injection.

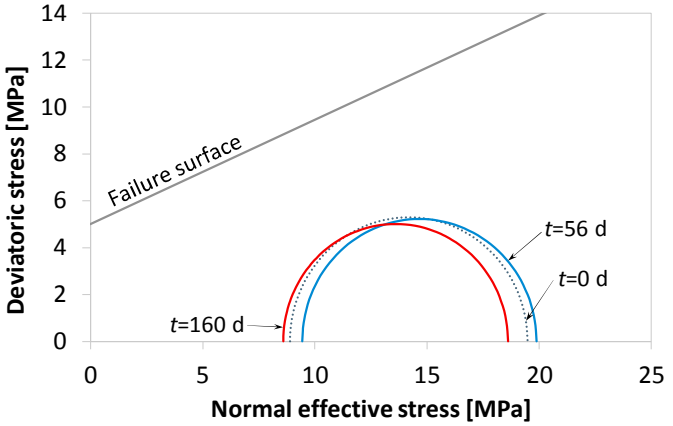

Figure 5. Evolution of caprock stability above the injection well, at a point placed 5 m above the reservoir-caprock interface, represented by Mohr circles before injection and after 56 and 160 days of CO_2 injection.

5.3. Fault stability

Unlike caprock stability, which is not compromised by CO_2 injection, the effective stress state reaches the yield surface in the fault core after 35 days of injection (Figure 6). Given the ductility of the fault core, which has a high clay content, the likelihood of inducing felt seismicity is low. In contrast, a series of very low magnitude microseismic events or aseismic slip is likely to occur [30]. Figure 6 shows that plastic strain accumulation in the fault core is progressive, being practically linear with time.

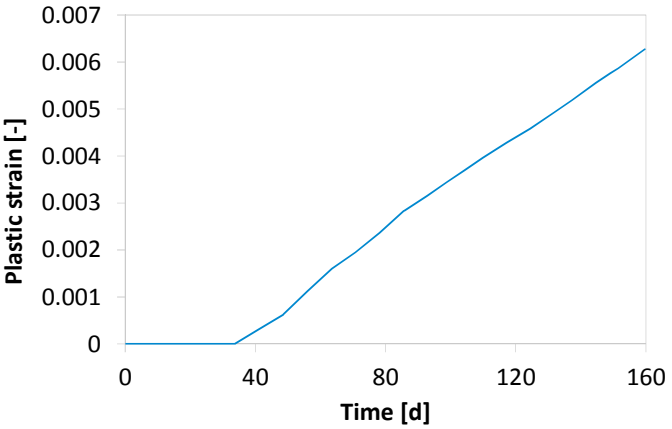

Figure 6. Plastic strain evolution in the fault core, at a point placed 7 m above the bottom of the reservoir.

Yield conditions are reached within the fault because its presence induces a complex stress redistribution in its vicinity when fluid injection occurs on one of its sides [31]. For the geometry of the problem, horizontal total stresses increase in the upper portion of the reservoir, in the region where the reservoir rock is placed on both sides of the fault. This increase occurs because reservoir rock is stiff and accumulates stresses. On the other hand, in the lower portion of the reservoir, where the base rock is placed on the other side of the fault, horizontal total stresses barely increase in response to reservoir pressurization because Opalinus clay (shale) is significantly more compressible than Berea sandstone. This small increase in the horizontal total stresses in the lower half of the reservoir maintains the deviatoric stress approximately constant during injection. Additionally, the increase in fluid

pressure reduces the effective stresses, displacing the Mohr circle towards the failure surface, which eventually leads to yielding of the fault.

6. Discussion and conclusions

We have simulated a generic CO_2 storage scenario modeling a stratified sedimentary formation, where high- and low-permeable layers are alternating, and added the crystalline basement at the bottom of the model. We have included a low-permeable fault that causes an additional pressure buildup, which may compromise both caprock and fault stability. We have also measured in the laboratory the properties of rocks representative of the modeled geomaterials. These measurements have been performed reproducing deep geological storage conditions. Using rock properties measured in the laboratory permits gaining confidence in describing the processes associated with fluid injection in the subsurface and discards certain risks that might be suspected when using generic properties.

The additional overpressure generated by the presence of a low-permeable fault gives rise to yielding of the fault. However, the caprock remains stable, which minimized the risk of CO_2 leakage across it. Despite the yielding of the fault, given its ductility, shear slip does not occur in a sudden single event that may induce felt seismicity, but rather in a slow progressive slip that may induce a sequence of microseismic events or aseismic slip without measurable seismicity. Even though such situation may not give rise to public concern, it should be minimized and controlled, because aseismic slip of portions of a fault may end up causing brittle failure in other sections [32].

Permeability of clay-rich geomaterials does not significantly increase after undergoing shear failure. Permeability increase may be of up to one order of magnitude, but still not enough to give rise to a significant fluid flow. Furthermore, the entry pressure of sheared clay-rich materials is still in the order of several MPa (Figure 4), so CO_2 will not be able to penetrate into it for the overpressures that are likely to be allowed at storage sites. Consequently, the risk of CO_2 leakage through ductile faults is low, even if they are reactivated. Still, the risk of pressurizing the crystalline basement is a concern, since it may give rise to induced felt seismicity, as has occurred in central US due to wastewater disposal in basal aquifers [33]. Were this to happen, the risk of CO_2 leakage would remain low because failure would occur deeper than the storage formation [8].

Acknowledgements

V.V. acknowledges financial support from the “TRUST" project (European Community's Seventh Framework Programme FP7/2007-2013 under grant agreement n. 309607) and from “FracRisk" project (European Community's Horizon 2020 Framework Programme H2020-EU.3.3.2.3 under grant agreement n. 640979). R.M. acknowledges partial support from the Center for Geologic Storage of CO_2, an EFRC funded by the U.S. DOE, Office of Science, BES, under Award DE-SC0C12504.

References

[1] De Simone, S., Vilarrasa, V., Carrera, J., Alcolea, A., and Meier, P. (2013). Thermal coupling may control mechanical stability of geothermal reservoirs during cold water injection. *Physics and Chemistry of the Earth, Parts A/B/C* 64: 117-126.

[2] Segall, P., and Lu, S. (2015). Injection-induced seismicity: Poroelastic and earthquake nucleation effects. *Journal of Geophysical Research: Solid Earth* 120(7): 5082-5103.

[3] Rutqvist, J., Rinaldi, A. P., Cappa, F., Jeanne, P., Mazzoldi, A., Urpi, L., Guglielmi, Y., and Vilarrasa, V. (2016). Fault activation and induced seismicity in geological carbon storage–Lessons learned from recent modeling studies. *Journal of Rock Mechanics and Geotechnical Engineering* 8(6): 789-804.

[4] Liu, L., Yu, Z., Yang, S., Li, S., and Yang, Y. (2012). An experimental study of CO_2–brine–rock interaction at in-situ pressure–temperature reservoir conditions. *Chemical Geology* 326-327: 88-101.

[5] Makhnenko, R.Y., Vilarrasa, V., Mylnikov, D., and Laloui, L. (2017). Hydromechanical aspects of CO_2 breakthrough into clay-rich caprocks. *Energy Procedia* 10.1016/j.egypro.2017.03.1453.

[6] Hitchon, B., Gunter, W. D., Gentzis, T., and Bailey, R. T. (1999). Sedimentary basins and greenhouse gases: a serendipitous association. *Energy Conversion and Management* 40(8): 825-843.

[7] Majer, E. L., Baria, R., Stark, M., Oates, S., Bommer, J., Smith, B., and Asanuma, H. (2007). Induced seismicity associated with enhanced geothermal systems. *Geothermics* 36(3): 185-222.

[8] Verdon, J. P. (2014). Significance for secure CO_2 storage of earthquakes induced by fluid injection. *Environmental Research Letters* 9(6): 064022.

[9] Carvalho, F.C.S., Chen, C.-N., and Labuz, J.F. (1997). Measurements of effective elastic modulus and microcrack density. *International Journal of Rock Mechanics & Mining Sciences*. 34:3-4, Paper No. 043.
[10] Makhnenko, R.Y., and Labuz, J.F. (2016). Elastic and inelastic deformation of fluid-saturated rock. *Philosophycal Transactions of Royal Society A* 374: 20150422.
[11] Räss, L., Makhnenko, R.Y., Podladchikov, Y., and Laloui, L. (2017). Quantification of viscous creep influence on storage capacity of caprock. *Energy Procedia* doi: 10.1016/j.egypro.2017.03.1455.
[12] Cassini, E., Mylnikov, D., and Makhnenko, R. (2017). Chemical influence of pore pressure on brine flow in clay-rich material. In: A. Ferrari and L. Laloui (eds), *Advances in Laboratory Testing and Modelling of Soils and Shales (ATMSS)*, Springer Series in Geomechanics and Geoengineering, 273-280.
[13] Gräsle, W. (2011). Multistep triaxial strength tests: investigating strength parameters and pore pressure effects on Opalinus clay. *Physics and Chemistry of the Earth* 36: 1898-1904.
[14] Labuz, J.F., and Biolzi, L. (1998). Characteristic strength of quasi-brittle materials. *International Journal of Solids & Structures* 35(31-32): 4191-203.
[15] IEAGHG. 2011. Caprock systems for CO_2 geological storage. *IEA Environmental Projects Ltd.*
[16] Hildenbrand, A., Schlömer, S., and Krooss, B.M. (2002) Gas breakthrough experiments on fine-grained sedimentary rocks. *Geofluids* 2: 3-23.
[17] Amann-Hildenbrand, A., Bertier, P., Busch, A., and Krooss, B.M., (2013). Experimental investigation of the sealing capacity of generic clay rich caprocks. *International Journal of Greenhouse Gas Control* 19: 620-641.
[18] Vilarrasa, V., and Carrera, J. (2015). Geologic carbon storage is unlikely to trigger large earthquakes and reactivate faults through which CO_2 could leak. *Proceedings of the National Academy of Sciences* 112(19): 5938-5943.
[19] Olivella, S., Gens, A., Carrera, J., and Alonso, E. E. (1996). Numerical formulation for a simulator (CODE_BRIGHT) for the coupled analysis of saline media. *Engineering Computations* 13(7): 87-112.
[20] Vilarrasa, V., Silva, O., Carrera, J., and Olivella, S. (2013). Liquid CO_2 injection for geological storage in deep saline aquifers. *International Journal of Greenhouse Gas Control* 14: 84-96.
[21] Burnside, N.M., and Naylor, M. (2014). Review and implications of relative permeability of CO_2/brine systems and residual trapping of CO_2. *International Journal of Greenhouse Gas Control* 23: 1-11.
[22] van Genuchten, M.T. (1980). A closed-form equation for predicting the hydraulic conductivity of unsaturated soils. *Soil Science Society of America Journal* 44: 892-898.
[23] Detournay, E., and Cheng, A. (1993). Fundamentals of poroelasticity. In Fairhurst, C. (ed.), Chap. 5, *Comprehensive Rock Engineering: Principles, Practice and Projects, Vol. II, Analysis and Design Methods*, Pergamon Press, Oxford; pp. 113–171.
[24] Makhnenko, R.Y., Harvieux, J., and Labuz, J.F. (2015). Paul-Mohr-Coulomb failure surface of rock in the brittle regime. *Geophysical Research Letters* 42: 6975-6981.
[25] Rohmer, J., Pluymakers, A., and Renard, F. (2016). Mechano-chemical interactions in sedimentary rocks in the context of CO_2 storage: Weak acid, weak effects? *Earth Science Reviews* 157: 86–110.
[26] Bennion, B., and Bachu, S. (2008). Drainage and imbibition relative permeability relationships for supercritical CO_2/brine and H_2S/brine systems in intergranular sandstone, carbonate, shale, and anhydrite rocks. *SPE Reservoir Evaluation & Engineering* 11(03): 487-496.
[27] Zhang, Z., and Agarwal, R. K. (2012). Numerical simulation and optimization of CO_2 sequestration in saline aquifers for vertical and horizontal well injection. *Computational Geosciences* 16(4): 891-899.
[28] Vilarrasa, V. (2014). Impact of CO_2 injection through horizontal and vertical wells on the caprock mechanical stability. *International Journal of Rock Mechanics & Mining Sciences* 66: 151-159.
[29] Hsieh, P. A. (1996). Deformation-induced changes in hydraulic head during ground-water withdrawal. *Ground Water* 34(6): 1082-1089.
[30] Cornet, F. H., Helm, J., Poitrenaud, H., and Etchecopar, A. (1997). Seismic and aseismic slips induced by large-scale fluid injections. In *Seismicity Associated with Mines, Reservoirs and Fluid Injections*, Birkhäuser, Basel; pp. 563-583.
[31] Vilarrasa, V., Makhnenko, R., and Gheibi, S. (2016). Geomechanical analysis of the influence of CO_2 injection location on fault stability. *Journal of Rock Mechanics and Geotechnical Engineering* 8(6): 805-818.
[32] Schmidt, D. A., Bürgmann, R., Nadeau, R. M., and d'Alessio, M. (2005). Distribution of aseismic slip rate on the Hayward fault inferred from seismic and geodetic data. *Journal of Geophysical Research: Solid Earth* 110: B08406.
[33] Ellsworth, W. L. (2013). Injection-induced earthquakes. *Science* 341(6142): 1225942.